

# How motility drives the glassy dynamics in confluent epithelial monolayers?

Souvik Sadhukhan,<sup>1,\*</sup> Manoj Kumar Nandi,<sup>2</sup> Satyam Pandey,<sup>1</sup> Matteo Paoluzzi,<sup>3</sup> Chandan Dasgupta,<sup>4,5</sup> Nir Gov,<sup>6</sup> and Saroj Kumar Nandi<sup>1,†</sup>

<sup>1</sup>Tata Institute of Fundamental Research, 36/P Gopanpally Village, Hyderabad - 500046, India

<sup>2</sup>Université Claude Bernard Lyon 1, Institut National de la Santé et de la Recherche Médicale, Stem Cell and Brain Research Institute, Bron 69500, France.

<sup>3</sup>Istituto per le Applicazioni del Calcolo del Consiglio Nazionale delle Ricerche, Via Pietro Castellino 111 80131 Napoli, Italy

<sup>4</sup>Department of Physics, Indian Institute of Science, Bangalore 560012, India

<sup>5</sup>International Centre for Theoretical Sciences, TIFR, Bangalore 560089, India

<sup>6</sup>Department of Chemical and Biological Physics, Weizmann Institute of Science, Rehovot 7610001, Israel

As wounds heal, embryos develop, cancer spreads, or asthma progresses, the cellular monolayer undergoes a glass transition from a solid-like jammed to a fluid-like flowing state. Two primary characteristics of these systems, confluency, and self-propulsion, make them distinct from particulate systems. Are the glassy dynamics in these biological systems and equilibrium particulate systems different? Despite the biological significance of glassiness in these systems, no analytical framework, which is indispensable for deeper insights, exists. Here, we extend one of the most popular theories of equilibrium glasses, the random first-order transition (RFOT) theory, for confluent systems with self-propulsion. One crucial result of this work is that, unlike in particulate systems, the confluency affects the effective persistence time-scale of the active force, described by its rotational diffusion  $D_r^{\text{eff}}$ . Unlike in particulate systems, this value differs from the bare rotational diffusion of the active propulsion force due to cell shape dynamics which acts to rectify the force dynamics:  $D_r^{\text{eff}}$  is equal to  $D_r$  when  $D_r$  is small, and saturates when  $D_r$  is large. We present simulation results for the glassy dynamics in active confluent models and find that the results are consistent with existing experimental data, and conform remarkably well with our theory. In addition, we show that the theoretical predictions agree nicely with and explain previously published simulation results. Our analytical theory provides a foundation for rationalizing and a quantitative understanding of various glassy characteristics of these biological systems.

## I. INTRODUCTION

The glassy nature of collective cellular dynamics in epithelial monolayers is crucial for many biological processes, such as embryogenesis [1–4], wound healing [5–8], cancer progression [9, 10]. One defining feature of glassiness is the rapid growth of relaxation time by several orders of magnitude, with a modest change in the control parameter [11, 12]. This enormous dynamical slow-down does not seem to accompany any apparent structural change in the static properties. However, there are several dynamical signatures, such as complex non-exponential relaxation [13, 14], dynamical heterogeneity [14, 15], caging [16], non-Gaussian particle displacements [17–19]. Although most of these glassy characteristics in biological systems are similar to those of non-living systems, there are crucial differences [20, 21]. These systems are active, that is, driven out of equilibrium. Activity has many different forms; for example, the constituents of such systems can divide and die [22–24], differentiate [25], be confluent [26, 27], be motile and self-propel [28, 29], etc. These properties are distinctive from those of non-living glassy systems and provide opportunities for fascinating discoveries and challenging theoretical di-

rections.

The effects of motility on the glassy dynamics of particulate systems are relatively well-understood [30–32]. These systems comprise self-propelled particles (SPPs) with a self-propulsion force,  $f_0$ , that has characteristic persistence time,  $\tau_p$  [28, 29]. The force persistence time  $\tau_p$  leads to a separation of time scales between the thermal and active dynamics. When  $\tau_p$  is not too large, an equilibrium-like description with an extended fluctuation-dissipation relation applies [33–37]. Due to the inherent complexities of these systems, simulation studies [38–41] and experiments on synthetic systems [42–44] have provided crucial insights. Theories of equilibrium glasses, such as the mode-coupling theory (MCT) [40, 45–49] or random first-order transition (RFOT) theory [50, 51], have been extended for active SPP systems. Surprisingly, many of the equilibrium glass properties survive in the presence of activity [21, 31, 45, 49], and the relaxation dynamics remain equilibrium-like at an effective temperature when  $\tau_p$  is not high. However, cellular monolayers and epithelial tissues, the systems of interest in this work, have a crucial difference from the particulate systems; they are confluent, that is, the particles fill the entire space and to date, no theory exists for the effect of motility on the glassy dynamics in such systems. Here, we develop a theoretical framework to understand how motility drives the glassy dynamics in confluent systems.

Several computational models exist to study the static and dynamical properties of confluent epithelial monolay-

\* ssadhukhan@tifrh.res.in

† saroj@tifrh.res.in

ers: for example, the cellular Potts model (CPM) [52–57], the Vertex model [26, 58–60], the Voronoi model [61–63], the phase-field model [64–66], etc. These models essentially vary in the details of implementations. Recent works have shown that all these models are similar from the perspective of the glassy dynamics, exhibiting a jamming transition from fluid-like fast dynamics to solid-like slow dynamics [57, 61, 62, 67, 68]. Note that this ‘jamming transition’ is distinct from the zero-temperature zero-activity jamming transition found in the physics of disordered systems [19, 31, 69] since here the jamming phenomenon essentially refers to the appearance of glassy dynamics. In confluent systems, the glassy dynamics have several unusual properties.

Compared to most particulate systems, confluent systems readily show sub-Arrhenius relaxation dynamics [57, 62, 68], and cellular shape is a crucial control parameter for these systems [61, 69]. These unusual properties make a theoretical description of the glassy properties in these systems challenging. In a recent work, some of us have phenomenologically extended one of the most popular theories of glassy dynamics, the random first-order transition (RFOT) theory [70–72], for a confluent monolayer of cells (lacking self-propulsion) [57]. The theoretical predictions agree well with the simulation results of equilibrium CPM in the absence of motility. However, cells are inherently out of equilibrium, and motility is crucial for cellular dynamics. In a seminal work, Bi *et al* have studied a minimal self-propelled Voronoi model [61] and showed that  $f_0$ ,  $\tau_p$  and the typical cell shape crucially affect the glassy behavior in these systems [61]. Thus, including motility within the analytical RFOT-inspired framework for confluent systems is essential. Crucially, as we show below, confluency has non-trivial effect on self-propulsion leading to novel phenomenology for the relaxation dynamics.

In this work, we extend the RFOT theory framework to understand how motility affects the glassy dynamics in confluent epithelial monolayers. The main results of the work are as follows: (1) We show that confluency has a non-trivial effect on the self-propulsion; specifically, it modifies the effective persistence time of the active forces, such that they differ from the intrinsic  $\tau_p$ . This is described by the modified rotational diffusivity  $D_r^{\text{eff}}$  arising from the coupling between shape and active force relaxation. (2) We extend the RFOT theory for confluent systems by adding the effects of self-propulsion and show that the theory agrees with our simulation results of active Vertex model. (3) We demonstrate that our extended RFOT theory rationalizes the existing simulation results for the active confluent systems and agrees quite well in determining the phase diagrams governing the glass transition from the solid-like jammed to fluid-like flowing state. These results illustrate that the effect of confluency on the self-propulsion is crucial for understanding how motility affects the glassy dynamics in confluent systems.

## II. MODELS FOR CONFLUENT CELL MONOLAYER

To set the notations, we first briefly describe the confluent models representing an epithelial monolayer. Experiments show that the height of a monolayer remains nearly constant [26]. Thus, a two-dimensional description, representing cells as polygons, is possible [59, 73, 74]. The computational models have two parts: the energy function and the way in which cells are defined in the model. The energy function,  $\mathcal{H}$ , describing a cellular monolayer is

$$\mathcal{H} = \sum_{i=1}^N \left[ \Lambda_A (A_i - A_0)^2 + \Lambda_P (P_i - P_0)^2 \right], \quad (1)$$

where  $N$  is the total number of cells in the monolayer,  $A_0$  and  $P_0$  are the target area and target perimeter, respectively.  $A_i$  and  $P_i$  are the instantaneous area and perimeter of the  $i$ th cell.  $\Lambda_A$  and  $\Lambda_P$  are area and perimeter moduli; they determine the strength with which the area and perimeter constraints in Eq. (1) are satisfied. The physical motivation behind the energy function,  $\mathcal{H}$ , is the following: We can treat the cell cytoplasm as an incompressible fluid [22]; therefore, the total cell volume is constant. Since the cellular heights in the monolayer remain nearly the same, cells want to have a preferred area,  $A_0$ .  $A_0$  can vary for different cells, but we have assumed it to be uniform for simplicity. On the other hand,  $P_0$  is a coarse-grained variable containing several effects. For most practical purposes, a thin layer of cytoplasm known as the cellular cortex determines the mechanical properties of a cell. Moreover, various junctional proteins, such as E-Cadherin,  $\alpha$ -Catenin,  $\beta$ -Catenin, tight-junction proteins, etc, determine cell-cell adhesion [22, 26, 75]. The properties of all these different proteins and the effect of the cell cortex lead to the perimeter term with a preferred perimeter, which is a balance of cortical contractility and cellular adhesion.

Multiplying the Hamiltonian with a constant does not affect any system property. Therefore, we can rescale length by  $\sqrt{A_0}$ , and write Eq. (1) as

$$\mathcal{H} = \sum_{i=1}^N \left[ \lambda_A (a_i - 1)^2 + \lambda_P (p_i - p_0)^2 \right], \quad (2)$$

where  $\lambda_A = \Lambda_A$ ,  $a_i = A_i/A_0$ ,  $\lambda_P = \Lambda_P/A_0$ ,  $p_i = P_i/\sqrt{A_0}$ , and  $p_0 = P_0/\sqrt{A_0}$ .  $A_0$  is the average area when we consider poly-disperse systems. One can also have a temperature  $T$  that represents various active processes as well as the equilibrium  $T$  [69] (see Appendix E for the details of implementation).  $p_0$  and  $T$  are the main control parameters of the system. In this work, we have used  $T = 0$  and study the athermal self-propelled system.

Using the energy function  $\mathcal{H}$ , we can calculate the force on a cell,  $\mathbf{F}_i = -\nabla_i \mathcal{H}$  (see Appendix E for more details of the implementation). For self-propulsion, we assign a

polarity vector,  $\hat{\mathbf{n}}_i = (\cos \theta_i, \sin \theta_i)$ , where  $\theta_i$  is the angle with the  $x$ -axis. We obtain the active force,  $\mathbf{f}_a = f_0 \hat{\mathbf{n}}_i = \mu v_0 \hat{\mathbf{n}}_i$ . We have set the friction coefficient  $\mu$  to unity.  $\theta_i$  performs rotational diffusion and is governed by the equation [61],

$$\partial_t \theta_i(t) = \sqrt{2D_r} \eta_i(t) \quad (3)$$

where  $\eta_i$  is a Gaussian white noise, with zero mean and a correlation  $\langle \eta_i(t) \eta_j(t') \rangle = \delta(t - t') \delta_{ij}$  and we have set the rotational friction coefficient to unity.  $D_r$  is the rotational diffusion coefficient that is related to a persistence time,  $\tau_p = 1/D_r$ , for the motility director of the cells.

Theoretical studies of the confluent cellular monolayers comprise analyzing the evolution of the system, with or without self-propulsion via various confluent models, either at zero or non-zero  $T$ . Some of the models are lattice-based discrete models, such as the Cellular Potts Model (CPM) [52–54], others are continuum models, such as the Vertex [26, 58, 60, 75] or the Voronoi model [61, 62, 76], and then there are models which have some elements of both, for example, the phase field models [64, 65]. One cellular process, the  $T1$  transition, is crucial for dynamics in these systems. In a  $T1$  transition, two neighboring cells move away, and other two cells become neighbors. It is also known as the “neighbor-switching” process [26, 60, 67]. In this work, we have simulated the Vertex model and the Voronoi model to test the theoretical predictions.

*The Vertex model:* Within the Vertex model, the vertices of the polygons representing the cells are the degrees of freedom [26, 60]. The cell perimeter connecting adjacent vertices is a line, either straight or with a constant curvature. One can simulate the model via either molecular dynamics (MD) [26, 60, 75] or Monte Carlo (MC) [77]; we have used MD in this work (see Appendix E for details). Within the Vertex model,  $T1$  transition is implemented externally: when an edge length becomes smaller than a predefined cutoff value,  $l_c$ , a  $T1$  transition is performed [60, 67]. After a successful  $T1$  transition, we increase the new length to  $\lambda_{T1}$  times  $l_c$  such that the same edge does not undergo immediate  $T1$  transition. We have used  $\lambda_{T1} = 2.0$ . Unless otherwise mentioned, for the results presented in this work, we have used a binary system,  $A_{0\alpha} = 1.2$  and  $A_{0\beta} = 0.8$ , with a 50 : 50 ratio such that the average area remains 1.0,  $l_c = 0.04$ . We start with a random initial configuration of cells and equilibrate the system for  $3 \times 10^5$  times before collecting the data. We averaged each curve for 100 time origins and 32 ensembles.

*Voronoi model:* In the Voronoi model, the degrees of freedom are the Voronoi centers of the polygons [61, 68, 76]. The tessellation of these Voronoi centers gives the polygons representing the cells. The  $T1$  transitions naturally occur in the Voronoi model, just like the CPM. We can use both MD and MC for the dynamics of the model; we have used the MC algorithm in this work [78]. The cell centers are moved stochastically by

an amount  $dr$  via the MC algorithm using Eq. (2). We perform the Voronoi tessellation at each time to construct the cells and calculate the updated area and perimeter. These updated values give the energy for the next step. Unless otherwise specified, we have used  $N = 100$  cells,  $dr = 0.25$ , and a random initial configuration. We equilibrate the system for  $10^5$  time steps before collecting data. We averaged each curve over 50 time origins and 32 ensembles.

### III. RESULTS

#### A. Effects of confluency on rotational diffusivity of self-propulsion

In confluent systems, the constituent particles are extended objects with no gap between neighboring cells. In these systems, cells can move only through shape changes of their boundaries. For the concreteness of our arguments, let us consider the Vertex model, although the discussion below holds in general. Within the Vertex model, cells move via the movement of the vertices. Persistent cellular movement will elongate the cell in that direction. This elongation of the cell takes time and depends on the properties of the surrounding system, since the movement of one cell must coordinate with that of other cells to keep the system confluent. We will show below that this leads to an effective rotational diffusivity,  $D_r^{\text{eff}}$ , of the self-propulsion forces. Active particles are associated with a director along which the active propulsion force,  $\mathbf{f}_a$  acts. By contrast, in confluent systems, when the internal propulsion force  $\mathbf{f}_a$  changes its direction, the forces exerted on the neighboring cells evolve as the cell deforms and elongates along the new force direction, which takes time. We now demonstrate the role of this elongation time,  $\kappa_l$ , and show that it leads to a modified, effective rotational diffusivity of the active forces,  $D_r^{\text{eff}}$ .

We first simulate a system long enough to reach the steady state. We then freeze the direction of  $\mathbf{f}_a$  for a chosen cell, and again reach steady state. This particular cell will elongate along the motile force direction. We then suddenly change the direction of  $\mathbf{f}_a$  of this cell. The cell will again start elongating along the new motile force direction (see Supplementary Movie). Immediately after switching the motile force direction, we measure the cell length as a function of time  $t$ ,  $l(t)$ , along the direction of  $\mathbf{f}_a$ , and going through the center of mass of the cell as schematically shown in Fig. 1(a). For better statistics, we also make the motile force magnitude of the chosen cell 16 times higher than the rest of the cells. The qualitative results do not depend on the higher magnitude of the motile force of this cell. We plot  $l(t)$  for various  $D_r$  of the system [Fig. 1(b)]. We see that  $l(t)$  reaches a steady state value that depends on  $D_r$ . We define a measure of the elongation time-scale,  $\kappa_l$ , when the cell reaches 0.9 of its steady state length.

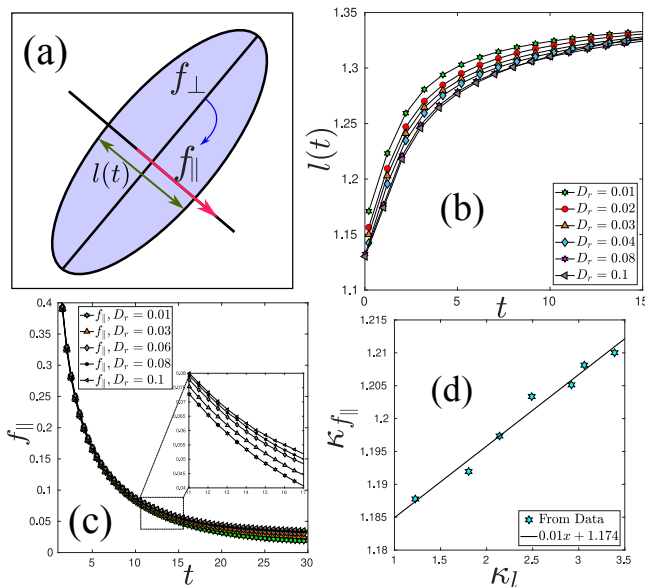


FIG. 1. Physical picture of the cellular elongation time,  $\kappa_l$ . (a) We freeze the direction of active force for a particular cell for a long-time and make the magnitude of the motile force 16 times higher for better statistics. The cell gets elongated along that direction. We then change the direction of the active force in perpendicular direction and measure the cellular length,  $l(t)$ , along that direction and the magnitude of forces,  $f_{\parallel}(t)$  and  $f_{\perp}(t)$ , as denoted in the figure. (b)  $l(t)$  for various values of  $D_r$ . We obtain the time scale  $\kappa_l$  when  $l(t)$  reaches 0.9 of its saturation value. (c) Relaxation of the force,  $f_{\parallel}(t)$ , along the direction of  $\mathbf{f}_a$  following the switching of active force direction. We obtain another time scale,  $\kappa_{f_{\parallel}}$ , when  $f_{\parallel}(t)$  relaxes to one fourth of its initial value. (d) The two time scales,  $\kappa_l$  and  $\kappa_{f_{\parallel}}$ , are proportional to each other. The straight line is for guide to eye. For these measurements, we have simulated 100 cells, used  $v_0 = 0.125$  and  $p_0 = 3.6$ , equilibrated the system for  $3 \times 10^5$  times before collecting data, and performed 32 ensembles and 1000 time averaging.

To understand the nature of the force within this elongation time-scale, we have also measured the average forces on the vertices of the cell along the direction of  $\mathbf{f}_a$  and perpendicular to it,  $f_{\parallel}(t)$  and  $f_{\perp}(t)$ , respectively.  $f_{\perp}$  remains nearly the steady state value, but  $f_{\parallel}$  is quite large right after the switch and it then decays over time [Fig. 1(c)]. We define another time-scale,  $\kappa_{f_{\parallel}}$ , when  $f_{\parallel}$  decays to half of its initial value. Fig. 1(d) shows that the two time scales,  $\kappa_l$  and  $\kappa_{f_{\parallel}}$ , are proportional. This establishes that the elongation time-scale is proportional to the time-scale of the active force changes inside the confluent system.

Now consider a scenario where we change the direction of the motile force for a particular cell every  $\tau_p$  time duration, on average. When  $\tau_p$  is much larger compared to  $\kappa_l$ , the cell will take a time  $\kappa_l$  to elongate along the direction of the active force. Therefore, there will be a delay in the cellular response, to be added to the persistence time of the internal active forces. On the other hand,

when  $\tau_p$  is small compared to  $\kappa_l$ , the cell cannot follow the rapid change of motile force direction, and the cellular elongation direction will change over a time-scale  $\kappa_l$ . Therefore, we can write the effective time-scale for the active force persistence time (and the change of the cell elongation axis) as the sum of these two time-scales

$$\tau_p^{\text{eff}} = \tau_p + \kappa_l. \quad (4)$$

Writing the time-scales in terms of diffusivities,  $\tau_p^{\text{eff}} = 1/D_r^{\text{eff}}$  and  $\tau_p = 1/D_r$ , we obtain

$$D_r^{\text{eff}} = \frac{D_r}{\kappa_l D_r + 1}. \quad (5)$$

Since  $D_r^{\text{eff}}$  is the effective diffusivity of the active forces (and cell elongations) that give the structural relaxation, in the formalism of extended RFOT theory for self-propulsion [50], Eq. (9) below, we must use  $D_r^{\text{eff}}$  instead of  $D_r$  for a confluent system. As we show below, this modification of  $D_r$  due to the constraint of confluency and finite cell elongation time is crucial for the dynamics of confluent systems in the presence of self-propulsion.

We now present our simulation results supporting this physical picture and analytical expression, Eq. (5). To follow the cell elongation direction, characterized by  $\phi(t)$ , we first calculate the gyration tensor for each cell and diagonalize it [69] to obtain two eigenvalues. The eigenvector corresponding to the major eigenvalue, i.e., the major axis direction  $\hat{\mathbf{s}}_i$ , gives  $\phi$  [Fig. 2(a)]. Note that  $\hat{\mathbf{s}}_i$  is *nematic* by nature as it corresponds to the cell elongation axis. We show in Fig. 2(b) the direction of the internal active force and that of  $\hat{\mathbf{s}}_i$  along a trajectory. Fig. 2(c) shows the direction change of the internal active force,  $\delta\theta$ , and that of  $\hat{\mathbf{s}}_i$ ,  $\delta\phi$ . Note that the magnitude of  $\delta\theta$  is much higher than that of  $\delta\phi$ . We obtain  $D_r^{\text{eff}}$  from the auto-correlation function of  $\delta\phi$ .

As discussed above,  $\kappa_l$  represents a time-scale for cell shape changes, and therefore we expect it to depend on the structural relaxation time  $\tau$  of the system (see Appendix E for a mathematical definition). For various  $p_0$  and  $v_0$ , we have first calculated  $\tau$  as a function  $D_r$  [Fig. 2(d)]. We then take a line of constant  $\tau$ , and for this set of parameters, we calculate the auto-correlation function,  $C_l(t)$ , given as

$$C_l(t) = \langle [\hat{\mathbf{s}}_i(t+t_0) \cdot \hat{\mathbf{s}}_i(t_0)]^2 \rangle, \quad (6)$$

where  $\langle \dots \rangle$  denotes averages over various cells, initial times  $t_0$ , and ensembles [79]. Note that the definition of  $C_l(t)$  in Eq. (6) takes into account the nematic nature of the major axis and  $C_l(t \rightarrow \infty) = 1/2$ . Fig. 2(e) shows the typical behavior of  $C_l(t)$ . From these plots, we obtain a time-scale,  $\tau_p^{\text{eff}}$ , by defining a cut-off value of  $C_l(t = \tau_p^{\text{eff}}) = 0.75$  and we obtain  $D_r^{\text{eff}} = 1/\tau_p^{\text{eff}}$ . Note that the definition of the cut-off value is arbitrary, and this introduces a scale in  $D_r^{\text{eff}}$ . We show the simulation data for  $D_r^{\text{eff}}$  as a function of  $D_r$  for two dif-

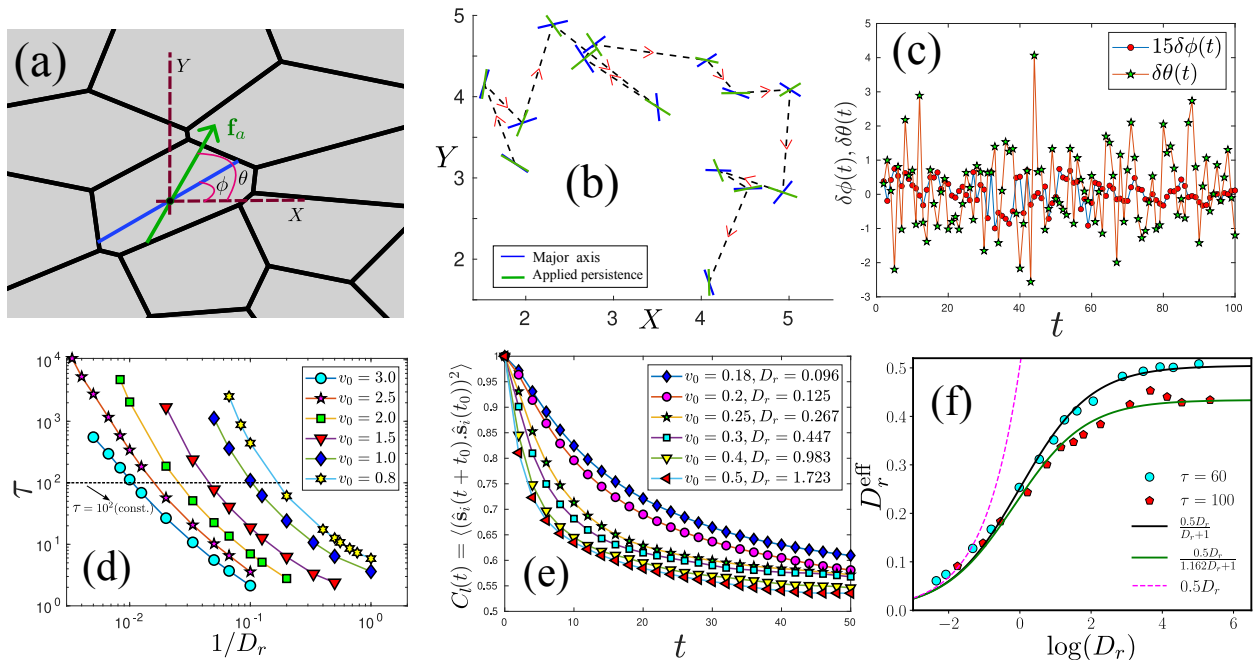


FIG. 2. Modification of rotational diffusivity in confluent systems. (a) A configuration of the cells in a dense confluent monolayer. Cells are always in contact with their neighbors. The blue line represents the major axis of the cell and the green arrow is the motile force direction. We schematically show the angles  $\theta$  and  $\phi$ . (b) We show the major axis (blue) and the sense of the active force (green) along the trajectory of a typical cell in the monolayer. The arrow indicates the direction of time. We have shown the configurations every  $10^3$  time step. (c)  $\delta\theta$  (green pentagram) corresponds to the angular variation of the active force, and  $\delta\phi$  (red circles) corresponds to that of the major axis. Note that we have multiplied  $\delta\phi$  by a factor of 15 to show in the same scale.  $\delta\phi$  varies much slower than  $\delta\theta$ . (d)  $\tau$  as a function of  $D_r^{-1}$  for different  $v_0$  and fixed  $p_0 = 3.72$ . From such plots, we obtain the values of different parameters that give a specific value of  $\tau$ . We have used  $N = 100$  cells for these simulations. (e) The auto-correlation function for the nematic order parameter  $\hat{s}_i$  (major axis). We keep  $p_0 = 3.72$  fixed, and use  $v_0$  and  $D_r$  such that  $\tau = 100$  (obtained from Fig. d). We define a cut-off as  $C_l(t = \tau_p^{\text{eff}}) = 0.75$  and obtain  $D_r^{\text{eff}} = 1/\tau_p^{\text{eff}}$ . (f)  $D_r^{\text{eff}}$  as a function of  $D_r$  obtained at two different  $\tau$ . The lines are the plot of our analytical argument [Eq. (5)].  $D_r^{\text{eff}}$  is proportional to  $D_r$  at small  $D_r$  and saturates at large  $D_r$ . The dashed line shows the behavior without the modification due to confluency.

ferent values of  $\tau$  in Fig. 2(f). We fit the data with  $D_r^{\text{eff}} = \Gamma D_r / (\kappa_l D_r + 1)$ , where  $\Gamma$  accounts for the arbitrary constant introduced by the cut-off value of  $C_l(t)$ . We have also used various other cut-off values in our analysis:  $\Gamma$  remains constant for a particular cut-off value. On the other hand,  $\kappa_l$  depends on the value of  $\tau$ . However, this dependence is not strong: we can ignore the  $\tau$  dependence when  $\tau$  becomes large. The solid lines in Fig. 2(f) show the comparison of the proposed analytical form [Eq. (5)], and the dashed line shows the behavior when we do not consider the modification due to confluency: the excellent agreement with the simulation data justifies the proposed analytical form. We use  $D_r^{\text{eff}}$  for the contribution coming from self-propulsion in the extended RFOT theory below.

## B. RFOT for the active confluent cell monolayer

The confluent models in the absence of self-propulsion are equilibrium systems. Although  $T$  in these models actually represents various energy-consuming active processes as well as equilibrium temperature, within the models it has the status of an equilibrium  $T$ . Such a description agrees well with experiments on systems where self-propulsion is small [14, 26, 52, 57, 80]. On the other hand, self-propulsion drives the system out of equilibrium. However, in the regime of small  $\tau_p$ , linear response still applies and we can define a generalized fluctuation-dissipation relation [36, 37, 69]. We consider a regime where  $\tau_p$  is not very large such that linear response remains applicable. In this regime, the relaxation dynamics remain equilibrium-like at an effective temperature  $T_{\text{eff}}$  [21, 45, 49]. Thus, we treat activity as a small perturbation [20, 50, 57]. The control parameters for the system are  $T$  and the three parameters of activity:  $p_0$  for confluency and  $v_0$  and  $\tau_p$  for self-propulsion.

RFOT theory posits that a glassy system consists of mosaics of glassy domains [70–72, 81, 82]. The typical length scale of these mosaics comes from a nucleation-like argument. The free energy cost for rearranging a mosaic of length  $R$  is

$$\Delta F = -\Omega_d R^d f + S_d R^\theta \Upsilon \quad (7)$$

where  $\Omega_d$  and  $S_d$  are the volume and surface area of a unit hypersphere in dimension  $d$ ,  $f$  is the free energy gain per unit volume, and  $\Upsilon$  is the surface free energy cost per unit area. The first term in Eq. (7) gives the free energy gain in the bulk, while the second term gives the cost at its surface due to mismatch. Within RFOT theory, configurational entropy,  $s_c(T)$ , is the driving force for the reconfiguration of mosaics and  $f = T s_c(T)$  at temperature  $T$ . Minimizing Eq. (7) yields the domain of length-scale,  $\xi = [\theta S_d \Upsilon / d \Omega_d T s_c]^{1/(d-\theta)}$ . We now discuss the effects of self-propulsion and confluency on  $\Upsilon$  and  $s_c$ .

We first consider the effects of activity on the configurational entropy,  $s_c[\Phi, T]$ , which is governed by the interaction potential  $\Phi$  and  $T$  [50, 83, 84]. We denote the potential energy of the passive system as  $\Phi_p$ , and that due to self-propulsion and confluency as  $\Phi_s$  and  $\Phi_c$ , respectively, and obtain  $s_c = s_c[\Phi_p + \Phi_s + \Phi_c, T]$ . As discussed above,  $\Phi_s$  is a small perturbation in the regime of our interest. The parameter  $p_0$  parameterizes  $\Phi_c$ . Although  $\Phi_c$  is not small for a confluent system, we can still use a perturbative expansion around a reference value.

The constraint of confluency leads to a geometric transition point along  $p_0$ . For a polygon of unit area, there is a specific minimum value of the perimeter,  $p_{\min}$ , but there is no limit on the maximum value. The ground state of a confluent system consists of hexagons, for which  $p_{\min} \simeq 3.712$ . In the case of disordered systems showing glassy dynamics,  $p_{\min}$  becomes slightly higher.  $p_{\min}$  has significant role in the static and dynamic properties of confluent systems. When  $p_0 > p_{\min}$ , the system can satisfy the perimeter constraint of Eq. (2), the cells have irregular sides represented by mostly concave polygons, and the system properties do not depend on  $p_0$ : this is known as the large- $p_0$  regime [57]. On the other hand, when  $p_0 < p_{\min}$ , the system cannot satisfy the perimeter constraint of Eq. (2), the cells have regular sides (straight or with constant curvature) represented by mostly convex polygons, and the system properties strongly depend on  $p_0$ : this is known as the low  $p_0$  regime [57]. We take a reference value of  $p_0$ ,  $p_0^{\text{ref}}$ , close to  $p_{\min}$  and determine its value via fitting to the simulation data. We take the potential corresponding to  $p_0^{\text{ref}}$  as a reference state and treat the potential around this value as a small parameter, i.e.,  $\Phi_c = \Phi_c^{\text{ref}} + \delta\Phi_c$  (see Appendix D for an alternative RFOT argument based on this  $p_0^{\text{ref}}$ ). Reference [57] has shown that such a description works well for confluent systems in the absence of self-propulsion. As shown

in the Appendix,  $\delta\Phi_c \propto (p_0 - p_0^{\text{ref}})$ , and we have

$$s_c[\Phi, T] \simeq \frac{\Delta C_p (T - T_K)}{T_K} + \chi_c (p_0 - p_0^{\text{ref}}) + \kappa_s \Phi_s, \quad (8)$$

where  $\Delta C_p$  is the specific heat difference between the liquid and crystalline phase,  $T_K$  is the Kauzmann temperature [85],  $\chi_c$  and  $\kappa_s$  are two constants.

Let us now consider the surface term. The temperature dependence of  $\Upsilon$  is linear [83]. Therefore,  $\Upsilon = \Xi(\Phi)T$ , where the interaction potential also governs the surface energy. For a system of SPPs close to the glass transition, the dominant contribution of self-propulsion comes from the bulk and enters the RFOT theory via  $s_c$  [50]. Assuming  $\Xi$  to be independent of  $v_0$  and  $\tau_p$  provides a good description of the behavior in such systems [50]. For simplicity, we keep this assumption also for active cell monolayer. On the other hand, confluency results in strong inter-cellular interaction at cell boundaries: this will affect  $\Xi$ . As detailed in the Appendix A [57], we have  $\Xi(\Phi_p, \Phi_c) = [B - C(p_0 - p_0^{\text{ref}})]$ , where  $B$  and  $C$  are two constants.

Within RFOT theory, relaxation dynamics occurs via the relaxation of individual mosaics [50, 70, 72]. The energy barrier associated with a region of length scale  $\xi$  is  $\Delta = \Delta_0 \xi^\psi$ , where  $\Delta_0$  is an energy scale, and  $\psi$  is another exponent. Considering a barrier-crossing scenario, we obtain the relaxation time as  $\tau = \tau_0 \exp[\Delta/k_B T]$ , where  $\tau_0$  is the relaxation time at high  $T$ . As detailed in the Appendix A, using  $\psi = \theta = d/2$  [70, 72, 83], we obtain

$$\ln\left(\frac{\tau}{\tau_0}\right) = \frac{E[1 - F(p_0 - p_0^{\text{ref}})]}{(T - T_K) + \chi(p_0 - p_0^{\text{ref}}) + \tilde{\kappa}_s \Phi_s} \quad (9)$$

where,  $\tilde{\kappa}_s = \frac{\kappa_s T_K}{\Delta C_p}$ ,  $\chi = \chi_c T_K / \Delta C_p$ ,  $F = C/B$ , and  $E = \frac{k\theta S_d T_K B}{\kappa_B d \Omega_d \Delta C_p}$  are all constants that we can obtain by fitting the equation with simulation or experimental data.  $\Phi_s$  is the effective mean potential energy due to self-propulsion, and we provide its detailed form below. We now confront our theory with new and existing simulation data.

### C. Comparison with simulation results of active Vertex model

We now compare the theoretical predictions with our simulation results of the active Vertex model (see Appendix E for simulation details). Fig. 3(a) shows a snapshot of the cells with the arrows indicating the self-propulsion direction. To characterize the dynamics, we compute the self-overlap function,  $Q(t)$ , as defined in Appendix E. We show the behavior of  $Q(t)$  for different values of  $v_0$  and fixed  $p_0$  and  $D_r$  in Fig. 3(b). The inset of Fig. 3(b) shows the behavior of the mean-square displacement,  $\Delta r^2(t)$  (defined in Appendix E). The plateau in  $Q(t)$  and sub-diffusive behavior in  $\Delta r^2(t)$  are typical

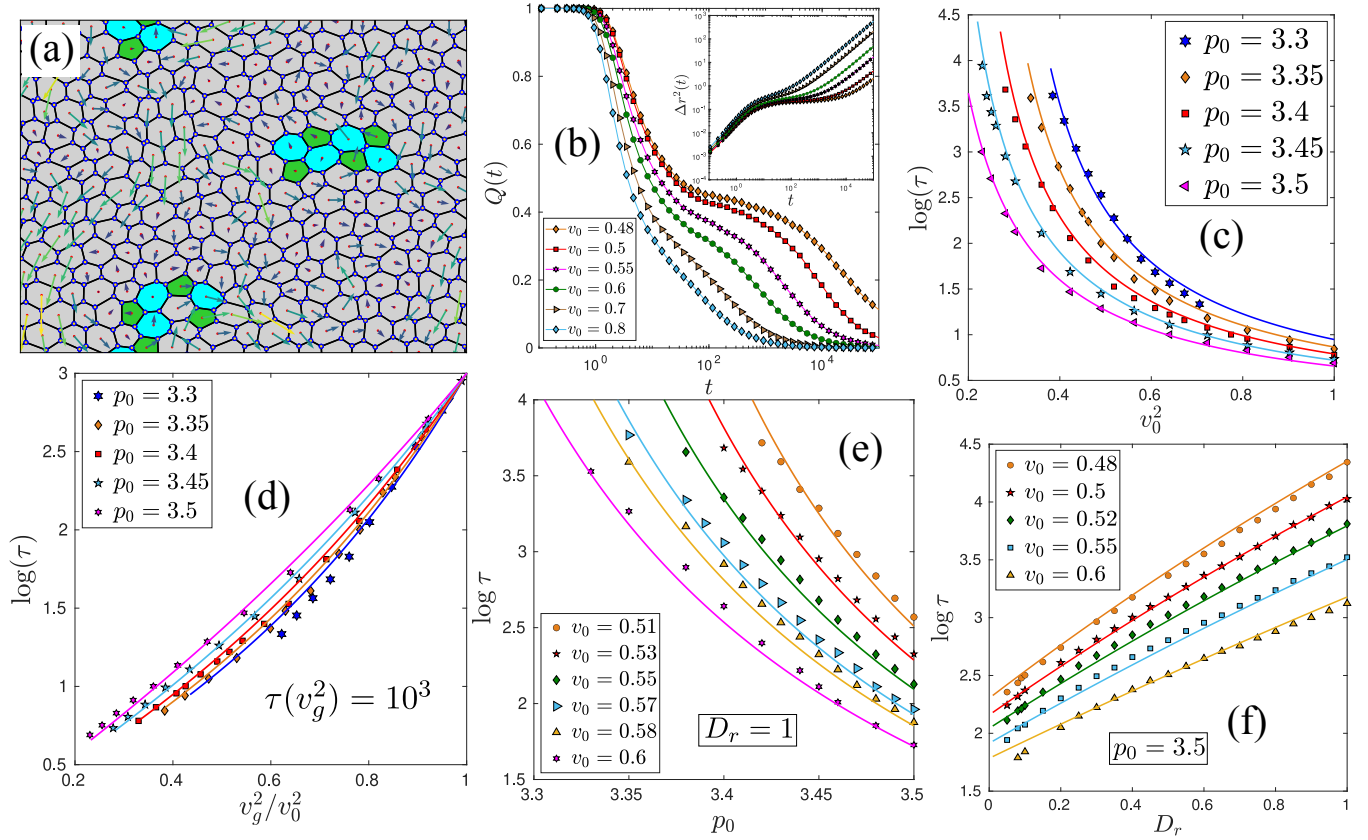


FIG. 3. Comparison of theoretical predictions with simulation results from the self-propelled Vertex model. (a) A typical configuration of the active Vertex model with  $p_0 = 3.5$ ,  $v_0 = 0.52$ , and  $D_r = 2.0$ . The arrowheads denote the velocity directions, and their lengths denote the magnitudes. Different colors indicate the number of vertices of the cells: green correspond to 5, gray to 6, and cyan to 7. (b) Self-overlap function,  $Q(t)$ , for different  $v_0$  with a fixed  $p_0 = 3.45$ , and  $D_r = 1$ . **Inset:** Mean square displacement for the same set of parameters as in the main figure. (c)  $\log \tau$  as a function of  $v_0^2$ : points are simulation data for different values of  $p_0$  and lines are the plot of Eq. (9) with the parameters given in the main text. (d) Angell plot representation of the data of Fig. (c). The system shows super-Arrhenius relaxation for this set of parameters. (e)  $\log \tau$  as a function of  $p_0$ : Points are simulation data for different values of  $v_0$  and lines are the theory. (f)  $\log \tau$  as a function of  $D_r$ : Points are simulation data for different values of  $v_0$  and lines are theory.

of glassy systems [11, 31]. We define the relaxation time  $\tau$  as  $Q(t = \tau) = 0.3$ . Fig. 3(c) shows the simulation results for  $\tau$  (symbols) as a function of  $v_0^2$  for different values of  $p_0$  and  $D_r = 1$ . To compare with the RFOT theory prediction, we first fix the parameters via fitting Eq. (9) with one set of data. Once these parameters are determined, there exist no other free parameters in the theory and we can then compare the model with the rest of the simulation data. Our simulation results suggest  $p_0^{\text{ref}} = 3.81$  which we have kept constant. As detailed in Ref. [50], considering a one-dimensional model for the dynamics of a single self-propelled particle in a confining potential with strength  $k$  and friction  $\gamma$ , we obtain

$$\Phi_s = \frac{Hv_0^2}{D_r^{\text{eff}} + G}, \quad (10)$$

where  $H = 1/\gamma$  and  $G = k/\gamma$ . Note that, as discussed in Sec. III A, we have used  $D_r^{\text{eff}}$  [Eq. (5)] instead of  $D_r$  in the expression of  $\Phi_s$  for a confluent system.

**Comparison for varying  $v_0$ :** Using the expression of  $D_r^{\text{eff}}$  in Eq. (9), for fixed  $p_0$  and  $D_r$  we obtain

$$\ln \left( \frac{\tau}{\tau_0} \right) = \frac{E' - F'(p_0 - 3.81)}{1 + \chi'(p_0 - 3.81) + Kv_0^2}, \quad (11)$$

where,  $E' = E/(T - T_K)$ ,  $F' = EF/(T - T_K)$ ,  $\chi' = \chi/(T - T_K)$ ,  $K = \tilde{\kappa}_s H / [\{\Gamma D_r / (\kappa_l D_r + 1) + G\}(T - T_K)]$ . Dividing the numerator and denominator of the right-hand side of Eq. (11) by  $K$ , we obtain

$$\ln \left( \frac{\tau}{\tau_0} \right) = \frac{\tilde{E} - \tilde{F}(p_0 - 3.81)}{\tilde{K} + \tilde{\chi}(p_0 - 3.81) + v_0^2}, \quad (12)$$

where,  $\tilde{E} = E'/K$ ,  $\tilde{F} = F'/K$ ,  $\tilde{\chi} = \chi'/K$ , and  $\tilde{K} = 1/K$ . The simulation results suggest a weak  $p_0$ -dependence in  $\tau_0$ . However, for simplicity, we take  $\tau_0 = 0.265$  as a constant. We obtain the rest of the parameters via fit with one particular set of data for  $p_0 = 3.35$ :  $\tilde{F} = 1.664$ ,

$\tilde{E} = 0.65$ ,  $\tilde{\chi} = 0.735$ , and  $\tilde{K} = 0.17$ . There are no other free parameters in the theory and we can compare the theoretical predictions with the simulation data, as shown in Fig. 3(c).

We now present the same data as in Fig. 3(c) in a way that is analogous to the well-known Angell plot [86, 87]. We define the glass transition point for the self-propulsion velocity,  $v_g$ , as  $\tau(v_g^2) = 10^3$ . Fig. 3(d) shows  $\log \tau$  as a function of  $v_g^2/v_0^2$ : the lines are the RFOT theory plot, obtained via Eq. (9) with the same parameters used in Fig. 3(c) and the symbols are simulation data. All the curves meet at  $v_0 = v_g$  by definition. The motivation behind plotting the data as a function of  $v_0^2$  instead of  $v_0$  is that  $v_0^2$  has the scale of temperature when  $D_r$  is constant. In the Angell plot representation, the diagonal line represents the Arrhenius relaxation. All the curves falling below this diagonal line signify super-Arrhenius relaxation.

**Comparison for varying  $p_0$ :** Next, we look at the dynamics as a function of  $p_0$ , keeping  $D_r$  and  $v_0$  fixed. For the comparison with the RFOT theory, we rewrite Eq. (9) as

$$\ln\left(\frac{\tau}{\tau_0}\right) = \frac{(\tilde{E} + 3.81\tilde{F}) - \tilde{F}p_0}{(\tilde{K} - 3.81\tilde{\chi} + v_0^2) + \tilde{\chi}p_0} = C' \frac{A' - p_0}{B' + p_0}, \quad (13)$$

where,  $C' = \tilde{F}/\tilde{\chi}$ ,  $A' = (\tilde{E} + 3.81\tilde{F})$ , and  $B' = (\tilde{K} - 3.81\tilde{\chi} + v_0^2)$ . Note that, in principle, all the parameters, such as  $\tau_0$ ,  $A'$ ,  $B'$ , and  $C'$  are known. However, since we obtained them via fit, there is always a scope of slight mismatch. To account for this, we use the previously determined values of the first three parameters and treat  $C'$  as a free parameter. We evaluate  $C'$  by fitting to one set of simulation data at  $v_0 = 0.51$ . We obtain the value of  $C' = 2.17$ , which is very close to the previously determined value  $C' = \tilde{F}/\tilde{\chi} \sim 2.26$ . We show in Fig. 3(e) that the theoretical predictions (lines) agree very well with the simulation data (symbols) at different values of  $v_0$ .

**Comparison for varying  $D_r$ :** We finally study the dynamics at varying  $D_r$ , keeping  $p_0$  and  $v_0$  fixed, and compare it with the RFOT theory. Note that the plateau height in  $Q(t)$  changes with varying  $D_r$ . Therefore, to study a range of  $D_r$ , we redefine  $\tau$  as  $Q(t = \tau) = 0.1$ . The definition does not change any of the physics. This implies that only  $\tau_0$  will change from the previous value. To compare the simulation data from the RFOT theory prediction, we write Eq. (9) as

$$\ln\left(\frac{\tau}{\tau_0}\right) = \frac{\tilde{E} - \tilde{F}(p_0 - 3.81)}{\tilde{K} + \tilde{\chi}(p_0 - 3.81) + \frac{v_0^2}{\frac{\Gamma D_r}{\kappa_l D_r + 1} + \tilde{G}}}, \quad (14)$$

where we have written the constants in such a way that  $\tilde{E}$ ,  $\tilde{F}$ ,  $\tilde{K}$ , and  $\tilde{\chi}$  remain the same as before and absorbed a constant factor in  $\tilde{\Gamma}$  and  $\tilde{G}$ . After straightforward al-

gebra, we get,

$$\ln\left(\frac{\tau}{\tau_0}\right) = \frac{\tilde{E} - \tilde{F}(p_0 - 3.81)}{\tilde{K} + \tilde{\chi}(p_0 - 3.81) + \frac{v_0^2(\kappa_l D_r + 1)}{\tilde{N} D_r + \tilde{G}}} \quad (15)$$

where,  $\tilde{N} = (\tilde{\Gamma} + \tilde{G}\kappa_l)$ . For comparison with the theory, we now need to determine the constants  $\kappa_l$ ,  $\tilde{N}$ , and  $\tilde{G}$  and  $\tau_0$  (due to the modified definition of  $\tau$ ). We obtain these parameters via fits to one dataset, for  $v_0 = 0.5$ . With a closer look, we expect  $\tilde{N}$  (due to the presence of the constant  $\tilde{\Gamma}$ ) and  $\tilde{G}$  to remain constant. However,  $\kappa_l$  and  $\tau_0$  can depend on  $v_0$ . We find that their dependence on  $v_0$  can be taken as linear:  $\kappa_l \simeq 0.98 - 1.26v_0$  and  $\tau_0 \simeq -3 + 7v_0$ . We obtain the other two constants as  $\tilde{N} \simeq 0.99$  and  $\tilde{G} = 0.78$ . With this set of parameters, Fig. 3(f) shows the comparison of simulation data (symbols) with the RFOT theory predictions (lines). Despite all these approximations involved in attaining Eq. (9), the agreement with simulation is remarkable.

#### D. Comparison with existing simulation results

We show that our extended RFOT theory also rationalizes the previously published simulation results on confluent systems. For this purpose, we chose the simulation data for the self-propelled Voronoi model from Bi *et al* [61]. Specifically, we compare the theory with the simulation results for the fluid-like to solid-like jamming or glass transition phase diagram. In [61] this transition was defined when the diffusion coefficient,  $D_{\text{eff}}$ , goes below  $10^{-3}$ . However, such a definition is not unique. Since the Stokes-Einstein relation for a suitably chosen  $\tau$  gives  $D_{\text{eff}}\tau = \text{const.}$  [12], we can equivalently define the glass transition via  $\tau$ . We therefore define the glass transition when  $\tau/\tau_0 = 10^6$ . As we show below, the functional form governing the phase diagram becomes independent of this specific form of the definition.

We use the expressions for  $\Phi_s$  [Eq. (10)] and  $D_r^{\text{eff}}$  [Eq. (5)] in Eq. (9), and obtain

$$\ln\left(\frac{\tau}{\tau_0}\right) = \frac{E[1 - F(p_0 - p_0^{\text{ref}})]}{(T - T_K) + \chi(p_0 - p_0^{\text{ref}}) + \frac{\tilde{\kappa}_s H v_0^2}{\kappa_l D_r + 1} + \tilde{G}}. \quad (16)$$

To compare the theory with the data of Ref. [61], we are interested in the phase diagram as functions of  $D_r$ ,  $v_0$ , and  $p_0$  at a fixed  $T$ . Therefore, we can treat  $T - T_K$  as a constant and write

$$\ln\left(\frac{\tau}{\tau_0}\right) = \frac{\tilde{E}[1 - F(p_0 - p_0^{\text{ref}})]}{1 + \tilde{\chi}(p_0 - p_0^{\text{ref}}) + \frac{\tilde{H} v_0^2}{\kappa_l D_r + 1} + \tilde{G}}, \quad (17)$$

where  $\tilde{E} = E/(T - T_K)$ ,  $\tilde{\chi} = \chi/(T - T_K)$  and  $\tilde{H} = \tilde{\kappa}_s H/(T - T_K)$ . Now, the definition of the glass transition,  $\tau/\tau_0 = 10^6$ , is independent of any control parameter value. Therefore, we can take  $p_0 = p_0^{\text{ref}}$  and  $v_0 = 0$  and

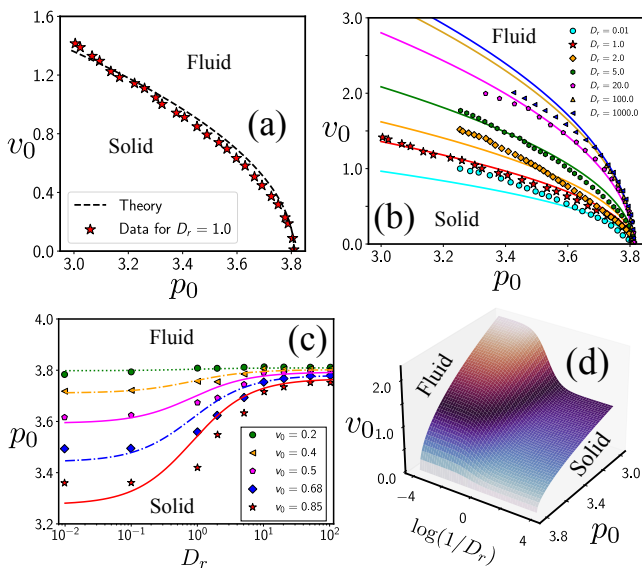


FIG. 4. Comparison of theoretical predictions with existing simulation data for the solid-like to fluid-like glass transition phase diagram. (a) We fit our theory, Eq. (19), to the simulation data of Ref. [61] and obtain the constants  $r = 1.138$ ,  $a = 0.798$  and  $b = 0.077$ . Symbols represent data from Ref. [61]; the dashed line is the fit. (b) Lines are the plots of Eq. (19), with the constants obtained from the fit shown in (a), for different values of  $D_r$ . Symbols are the corresponding simulation data taken from Ref. [61]. (c) Theoretical predictions for phase diagram in  $p_0 - D_r$  plane for different values of  $v_0$  and symbols are the corresponding simulation data taken from Ref. [61]. Note that the values of  $v_0$  used here are *different* from those in Ref. [61] (see text). Lines are the plot of Eq. (19). (d) 3d phase diagram for the active cell monolayer.

obtain  $\bar{E} = 6 \ln 10$ . Therefore, from Eq. (17), we obtain

$$\bar{K}(p_0^{\text{ref}} - p_0) = \frac{\bar{H}v_0^2}{\frac{\Gamma D_r}{\kappa_l D_r + 1} + G}, \quad (18)$$

where  $\bar{K} = \tilde{\chi} + F$ . Therefore, the phase boundary governing the solid-like to fluid-like jamming transition is determined by the following equation:

$$(p_0^{\text{ref}} - p_0) = \frac{v_0^2}{r + \frac{D_r}{bD_r + a}}, \quad (19)$$

where we have redefined the constants as  $r = G\bar{K}/\bar{H}$ ,  $a = \bar{H}/\Gamma\bar{K}$ , and  $b = \kappa_l\bar{H}/\Gamma\bar{K}$ . The analysis of the data from Ref. [61] suggests  $p_0^{\text{ref}} = 3.81$ . We obtain the three parameters,  $r$ ,  $a$ , and  $b$ , by fitting Eq. (19) with one set of simulation data (Fig. 2(a) of Ref. [61] for  $D_r = 1$ ):  $a = 0.798$ ,  $b = 0.077$ , and  $r = 1.138$ . Fig. 4(a) shows the corresponding plot. Once these constants are determined, there are no other free parameters. We can now compare our theory with the other sets of data from Ref. [61].

We show in Fig. 4(b) the theoretical predictions (lines)

for the solid-like to fluid-like phase boundary in the  $v_0 - p_0$  plane for different values of  $D_r$  and also the simulation data by symbols taken from Fig. 3(a) of Ref. [61]. Here, we emphasize two points: first, the theoretical curves are *not* fits to the simulation data; they are the *predictions* of the theory given the values of the three constants obtained from the fit in Fig. 4(a). Similar phase diagrams in the  $v_0 - p_0$  plane have been reported in Refs. [75, 76] for different realizations of active cell monolayer. Second, such an agreement with the simulation data is impossible without including the effects of confluency on the self-propulsion via Eq. (5). Thus, confluency strongly modifies the effective self-propulsion of the system.

Next, we look at the behavior of the critical value of  $p_0$  as a function of  $D_r$  for different values of  $v_0$  and compare the theory with the simulation data presented in Fig. (3b) of Ref. [61]. We plot our theoretical *predictions* as lines in Fig. 4(c), and the corresponding simulation data (symbols) are from Ref. [61]. We note here that the values of  $v_0$  used in this plot are *different* from those presented in Ref. [61]. We have chosen  $v_0$  such that the theoretical curves match the simulation data. These values of  $v_0$  are consistent with the expected values from the other figures in Ref. [61]. The critical value of  $p_0$  saturates in both limits when  $D_r \rightarrow 0$  and  $D_r \rightarrow \infty$  and agrees well with Eq. (19); in the former case, it saturates to  $3.81 - v_0^2/r$ , and in the latter case, it saturates to a value  $3.81 - v_0^2/(r + 1/b)$ . Summarizing all these results, we can present the solid-like to fluid-like transition in a 3d phase diagram from Eq. (19). We show this phase diagram in Fig. 4(d), and find that it is remarkably similar to the phase diagram of Bi *et al.* (Fig. 3(c) of Ref. [61]). Thus, our theory rationalizes these simulation results.

#### IV. DISCUSSION

To conclude, we have extended the RFOT theory of equilibrium glasses for a confluent system of a cellular monolayer with self-propulsion. We have compared our theoretical predictions with new and existing simulation data, and show that our theory captures the primary characteristics of the glass transition from the solid-like jammed to the fluid-like flowing states in such systems. Understanding the effect of motility on the glassy dynamics of confluent systems is crucial for many biological processes. Our work provides a theoretical framework to understand the nontrivial nature of relaxation dynamics in these systems. Theoretical studies till now have treated the two crucial aspects of biological systems, confluency [57, 69], and motility [21, 46, 47, 49–51], separately. Here, for the first time, we have included both aspects within a single theoretical framework and reveal novel features of motility-driven glassy dynamics in confluent epithelial systems.

The crucial result of this work is that confluency modifies the effective persistence time of self-propulsion. This

modification appears as an effective rotational diffusivity,  $D_r^{\text{eff}}$  of the active propulsion forces. In cellular systems, a cell needs time to elongate along the changing direction of the active force, and this elongation time,  $\kappa_l$ , should depend on both  $f_0$  (or  $v_0$ ) and  $\tau$  of the system. We have shown in our simulations that  $\kappa_l$  relates the time scale of active force relaxation as well as that of the cellular elongation. Using  $\kappa_l$ , we have phenomenologically obtained an analytical expression for the modified diffusivity of the active force  $D_r^{\text{eff}}$  and verified it in our simulation.

Analysis of the relaxation dynamics of existing and new simulation results seem to suggest that  $D_r^{\text{eff}}$  is crucial for confluent cellular systems. We have shown in Fig. 6 that one cannot explain the simulation results for the relaxation dynamics without considering  $D_r^{\text{eff}}$ . In the experimental context, one can vary the cellular activity through different oncogenes, such as the Ras [88], or via growth factors, such as the protein kinase C [89]. For example, a tumor suppressor protein, Merlin, increases directional persistence and reduces motility force in Madin–Darby canine kidney (MDCK) dog epithelial cells [? ]. However, the change in the dynamics should be less sensitive to the change in  $\tau_p$  at when persistence is high due to the effect of confluency where  $D_r^{\text{eff}}$  becomes nearly constant when  $D_r$  is large.

Within the theoretical descriptions of confluent systems via Eq. (2),  $p_0$  parameterizes inter-cellular interaction. The phase diagrams in Fig. 4 suggest that the system remains fluid beyond a specific value of  $p_0$ . The parameter  $p_0^{\text{ref}}$  in Eq. (19) is crucial in obtaining this behavior. Our theory does not predict  $p_0^{\text{ref}}$ ; it is an input. We provide an alternate argument in Appendix D for the extended RFOT theory for confluent systems based on  $p_0^{\text{ref}}$ . The value of  $p_0^{\text{ref}}$  seems to vary for different systems and depends on the details of the models. It is possibly related to the geometric constraint leading to  $p_{\text{min}}$ .  $p_0^{\text{ref}}$  seems to control the glassy dynamics in confluent systems, and it is critical to understand what leads to  $p_0^{\text{ref}}$  and how it affects the dynamical behavior.

The glassy behavior with changing self-propulsion velocity,  $v_0$ , seems similar to that in particulate systems where increasing  $v_0$  fluidizes the system. However, the behavior with varying  $D_r$  seems non-trivial, where the plateau height in  $Q(t)$  seems to vary. This behavior generally signifies a variation in caging length. We will explore this aspect in more detail later. The other aspect, specific to confluent systems, is the fluidization with increasing  $p_0$  even when  $p_0$  is much lower than  $p_0^{\text{ref}}$ . As shown in Fig. 3(e),  $\tau$  decreases with increasing  $p_0$ . Experiments seem to agree with this result [27, 90]. For example, Ref. [8] have shown that expression of RAB5A, a key endocytic protein, produces large-scale motion and fluidizes a solid-like jammed tissue of human mammary epithelial MCF-10A cells. RAB5A enhances endosomal trafficking and macropinocytic internalization and, thus, facilitates the dynamics of cellular junctional proteins, reducing inter-cellular interaction. This effect implies an increase in  $p_0$  that leads to fluidization, much like the

results of Fig. 3(e).

Apart from their biological significance, the glassy dynamics in confluent systems is interesting from the perspective of theories of glassy systems. The confluent systems provide a rich testing ground for various theories of glassy dynamics. They can be viewed as limiting systems for the highly dense aggregates of soft particles. The glassy dynamics in dense systems of soft particles show several intriguing properties, such as super-diffusive behavior [91] or sub-Arrhenius relaxation [92–94]. Such behaviors are abundant in confluent systems [14, 57, 68]. Specifically, the sub-Arrhenius relaxation in these systems seems to result in a negative  $T_K^{\text{eff}}$  implying a finite relaxation time even at zero  $T$ . Based on this result, we can define a  $p_0^{\text{ref}}$  and develop the RFOT arguments as in Appendix D. These arguments show that the relaxation should become super-Arrhenius at lower values of  $p_0$  [57]. We have verified this prediction for the cellular Potts model in Ref. [57] and for the Voronoi and the Vertex models here (Appendix B). In our simulation, we have chosen the parameters such that we are in the super-Arrhenius regime (Fig. 3). On the other hand, the sub-Arrhenius regime seems to be nearly ideal for the mode-coupling theory of glassy dynamics [95]. How the same system crosses over from one mechanism to the other for the relaxation dynamics and if it is similar in equilibrium systems remain fascinating questions.

Finally, our work provides a foundation for a deeper understanding of the fascinating glassy aspects of confluent systems, both from biological and theoretical perspectives. There are many critical questions in this direction. It is well-known that cell shape is closely related to dynamics in confluent systems [69, 80, 96]. It will be intriguing to include metrics of cell shape within the RFOT theory framework to study how the dynamics and statics are connected. Moreover, cellular shapes are also related to functions. Such a framework will allow us to analyze shape, dynamics, and function within a single framework. Besides, perturbing one particular protein in a biological system can have multiple effects. A detailed understanding of how various parameters affect the dynamic behavior can reveal the actual consequences of such perturbations in experiments and eventually allow us to design diverse gene-level manipulations to target specific aspects of the system.

We have shown that the extended RFOT theory captures several glassy aspects in confluent models of epithelial systems. The main ingredients of the theory are (1) the mosaic-like nature whose length-scale comes from the competition of surface and bulk free energies leading to a nucleation-like scenario, (2) the geometric constraint leading to a reference state, given by  $p_0^{\text{ref}}$ , and (3) the modified  $D_r^{\text{eff}}$  of the active force, due to its coupling with cell elongation, that allows structural relaxation. Using new and existing simulation data, we have tested the predictions against two distinct models of confluent systems, the Vertex model (Fig. 3) and the Voronoi model (Fig. 4). Therefore, we believe the theory should be applicable

in general, including particle-based models of confluent monolayers [97, 98].

### ACKNOWLEDGMENTS

We thank Daniel Sussman for sharing the data of  $\tau$  for bidisperse Voronoi model from Ref. [68]. SS thanks ‘‘Infosys-TIFR Leading Edge Travel Grant’’, Ref.No.: TFR/Efund/44/Leading Edge TG(R-3)/09/ for the funding for travel to Israel. MP acknowledges NextGeneration EU (CUP B63C22000730005) within the Project IR0000029 - Humanities and Cultural Heritage Italian Open Science Cloud (H2IOSC) - M4, C2, Action 3.1.1. We acknowledge the support of the Department of Atomic Energy, Government of India, under Project Identification No. RTI 4007. S.K.N. thanks SERB for grant via SRG/2021/002014.

### Appendix A: Details of the RFOT theory calculation

As discussed in the main text, both the configurational entropy,  $s_c$ , and the surface energy are functions of the interaction potential of the system [50, 84]. For our system, we write the total interaction potential as sum of three distinct contributions:  $\Phi_p$  for the passive system,  $\Phi_s$  for the self-propulsion, and  $\Phi_c$  for confluency. Thus,  $s_c = s_c[\Phi_p + \Phi_s + \Phi_c]$  and  $\Xi = \Xi[\Phi_p + \Phi_s + \Phi_c]$ . We assume that self-propulsion, and hence  $\Phi_s$ , is low and a generalized fluctuation-dissipation relation is valid. For a confluent system,  $\Phi_c$  itself cannot be small as the system remains confluent at all times. The interaction potential is parameterized by  $p_0$ . We assume a reference state given by  $p_0^{\text{ref}}$  and the corresponding value of potential as  $\Phi_c^{\text{ref}}$ . Thus,  $\Phi_c = \Phi_c^{\text{ref}} + \delta\Phi_c$ , where  $\delta\Phi_c$  is small. Therefore, we have

$$s_c[\Phi, T] = s_c[\Phi_p + \Phi_c^{\text{ref}}] + \left. \frac{\delta s_c}{\delta \Phi_c} \right|_{(\delta\Phi_c, \Phi_s)=0} \delta\Phi_c + \left. \frac{\delta s_c}{\delta \Phi_s} \right|_{(\delta\Phi_c, \Phi_s)=0} \Phi_s + \dots, \quad (\text{A1})$$

where  $s_c[\Phi_p + \Phi_c^{\text{ref}}]$  is the configurational entropy of the reference system,  $\delta s_c/\delta \Phi_c|_{(\delta\Phi_c, \Phi_s)=0}$  and  $\delta s_c/\delta \Phi_s|_{(\delta\Phi_c, \Phi_s)=0}$  are constants. We assume the reference system follows the RFOT theory: the configurational entropy vanishes at the Kauzmann temperature  $T_K$ . Therefore, we can write  $s_c$  close to  $T_K$  as  $s_c[\Phi_p + \Phi_c] = \frac{\Delta C_p(T - T_K)}{T_K}$ , where  $\Delta C_p$  is the difference in specific heat between the liquid and the periodic crystalline phase [85].

The interaction energy in confluent systems is given by the perimeter term, and we can write [57]  $\delta\Phi_c \propto (p_0 - p_0^{\text{ref}})$ . Therefore, we have  $\delta s_c/\delta \Phi_c|_{(\delta\Phi_c, \Phi_s)=0} \delta\Phi_c = \chi_c(p_0 - p_0^{\text{ref}})$ , where  $\chi_c$  is a constant. Then, we can write

$s_c[\Phi, T]$  as

$$s_c[\Phi, T] \simeq \frac{\Delta C_p(T - T_K)}{T_K} + \chi_c(p_0 - p_0^{\text{ref}}) + \kappa_s \Phi_s, \quad (\text{A2})$$

where  $\kappa_s = \delta s_c/\delta \Phi_s|_{(\delta\Phi_c, \Phi_s)=0}$  is another constant. On the other hand, following Ref. [50], we ignore the contribution of  $\Phi_s$  to the surface reconfiguration energy, thus  $\Xi = \Xi[\Phi_p, \Phi_c^{\text{ref}} + \delta\Phi_c]$ . Expanding the effect of confluency around the reference state, we obtain

$$\Xi[\Phi] \simeq \Xi[\Phi_p, \Phi_c^{\text{ref}}] + \left. \frac{\delta \Xi}{\delta \Phi_c} \right|_{\delta\Phi_c=0} \delta\Phi_c + \dots \quad (\text{A3})$$

Using similar arguments as above, we can write  $\Xi[\Phi] \simeq B - C(p_0 - p_0^{\text{ref}})$ .

As shown in the main text, the typical length scale of the mosaics is

$$\xi = \left[ \frac{\theta S_d \Upsilon}{d \Omega_d T s_c} \right]^{1/(d-\theta)}. \quad (\text{A4})$$

Relaxation within RFOT theory is described by the relaxation of the individual mosaics. Considering a barrier-crossing scenario, we have the relaxation time  $\tau$

$$\tau = \tau_0 e^{\Delta_0 \xi^\psi}, \quad (\text{A5})$$

where  $\Delta_0$  is an energy scale and  $\tau_0$  is the high  $T$  relaxation time. Substituting the value of  $\xi$  above, we get

$$\ln\left(\frac{\tau}{\tau_0}\right) = \frac{\Delta_0}{k_B T} \left[ \frac{\theta S_d \Upsilon}{d \Omega_d T s_c} \right]^{\frac{\psi}{d-\theta}}. \quad (\text{A6})$$

Using the expressions of  $\Upsilon$  and  $s_c$ , and  $\psi = \theta = d/2$  [70, 72, 83], we obtain,

$$\ln\left(\frac{\tau}{\tau_0}\right) = \frac{E[1 - F(p_0 - p_0^{\text{ref}})]}{(T - T_K) + \chi(p_0 - p_0^{\text{ref}}) + \tilde{\kappa}_s \delta\Phi_s}, \quad (\text{A7})$$

where,  $E = k\theta S_d T_K B / k_B d \Omega_d \Delta C_p$ ,  $\tilde{\kappa}_s = \kappa_s T_K / \Delta C_p$ ,  $\chi = \chi_c T_K / \Delta C_p$  and  $F = C/B$ .

### Appendix B: The RFOT theory prediction of super- and sub-Arrhenius regimes in confluent systems

One unusual aspect of the glassy dynamics in confluent systems is the readily found sub-Arrhenius relaxation dynamics: In the Angell plot representation [86, 87], plotting  $\log \tau$  as a function of  $T_g/T$ , where  $T_g$  is the glass transition temperature, a straight line represents the Arrhenius relaxation, that is  $\tau$  grows as an exponential of  $1/T$ . When relaxation is super-Arrhenius, i.e., faster than exponential, the curve appears below the straight line. In contrast, when relaxation is sub-Arrhenius, i.e., slower than exponential, it appears above the straight line. All the models of confluent systems, the Vertex model, the Voronoi model [68], and the CPM [57] show

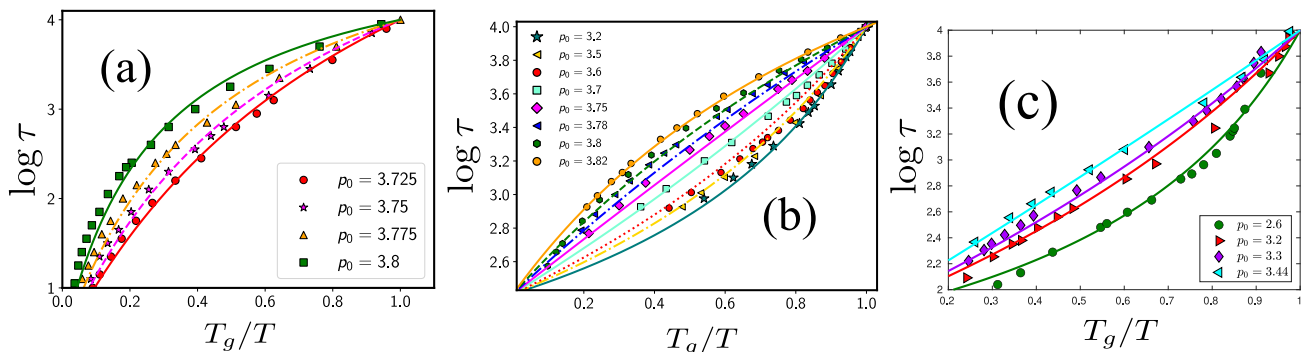


FIG. 5. The Angell plot-representation of the relaxation time for various systems. (a) Passive bi-disperse Voronoi model. Simulation data taken from Ref. [68]. (b) Data for a mono-disperse Voronoi model with a wide range of  $p_0$  values. (c) Simulation results for the passive Vertex model. In all the figures, symbols represent simulation data, and the dotted lines are RFOT theory predictions [Eq. (B1)]. See the text for the parameters for each of these plots.

sub-Arrhenius behavior for certain values of the parameters. The extended RFOT theory for the glassy dynamics in confluent systems [57] predicts that  $T_K^{\text{eff}}$ , the effective Kauzmann temperature, becomes negative in the sub-Arrhenius regime. This result suggests that  $\tau$  does not diverge even at zero  $T$ . On the other hand, Ref. [95] showed that another theory, the mode-coupling theory (MCT), applies remarkably well in this regime and  $\tau$  diverges at a finite  $T$  as a power law.

On the other hand, the extended RFOT theory also predicts the presence of super-Arrhenius relaxation at lower  $p_0$  values [57]. This prediction has been tested for the CPM [57] and the Voronoi model [62]. In the main text, we have shown that the super-Arrhenius regime exists in the self-propelled Vertex model. Here we show that this specific prediction is also valid for the equilibrium Vertex model and provide detailed comparison of the RFOT theory for the equilibrium Voronoi and Vertex models..

For the passive systems, the RFOT expression, Eq. (9), becomes

$$\ln \left( \frac{\tau}{\tau_0} \right) = \frac{k_1 - k_2(p_0 - p_0^{\text{ref}})}{T - T_K + \chi(p_0 - p_0^{\text{ref}})}, \quad (\text{B1})$$

where  $k_1 = E$  and  $k_2 = EF$ . We first compare the theory with the existing Voronoi model simulation data presented in Ref. [68]. We find that  $p_0^{\text{ref}} = 3.53$  gives a good description of the simulation data, and fitting Eq. (B1) with one set of data, we find  $\tau_0 = 2.323$ ,  $k_1 = 0.166$ ,  $k_2 = 0.220$ ,  $T_K = 0.000146$  and  $\chi = 0.04$ . Fig. 5(a) shows the comparison of the theory (lines) with the simulation data of Ref. [68] (symbols). Using these values of the constants, it is easy to verify that  $T_K^{\text{eff}} = T_K - \chi(p_0 - p_0^{\text{ref}})$  becomes negative for these set of curves in Fig. 5. This is consistent with the fact that the curves represent sub-Arrhenius behaviors.

According to the RFOT theory, we expect the behavior to become super-Arrhenius at lower  $p_0$ , however, Sussman *et al* did not explore this regime [68]. Since the de-

tailed values of the parameters depend on the specific system, to test this aspect, we first present simulation data for the equilibrium Voronoi model for a range of  $p_0$  values showing both the super- and sub-Arrhenius behavior. For our system with  $\lambda_A = 1.0$ ,  $\lambda_P = 1.0$ , and  $N = 100$ , we find  $p_0^{\text{ref}} = 3.72$ ,  $\tau_0 = 5.545$ ,  $k_1 = 0.064$ ,  $k_2 = 0.112$ ,  $T_K = 0.002$  and  $\chi = 0.087$ . We show the comparison of our simulation data with Eq. (B1) in Fig. 5(b). Consistent with the results of Ref. [68], the relaxation dynamics is sub-Arrhenius for the range of  $p_0 = 3.82 - 3.75$ , and then the dynamics becomes super-Arrhenius for lower  $p_0$ , as also found in Ref. [62].

We finally present our simulation results for the equilibrium Vertex model testing the prediction for the super-Arrhenius behavior at lower  $p_0$  values. For these simulations, we have used the open-source software RheoVM [99] to simulate the Vertex model via Brownian dynamics. We have used a system size of  $30 \times 30$  with  $N = 400$  cells, preferred area  $A_0 = L^2/N$ ,  $\lambda_A = 0.5$ , and  $\lambda_P = 0.05$ . We take the friction coefficient for the Brownian dynamics as 0.1. For the clarity of presentation, we only show the super-Arrhenius behavior for the lower values of  $p_0$  in Fig. 5(c). Our analysis suggests the value of  $p_0^{\text{ref}} = 3.45$ . Fitting one set of data gives the values of the constants in Eq. B1 as follows:  $\tau_0 = 4.164$ ,  $k_1 = 0.0381$ ;  $k_2 = 0.0056$ ,  $T_K = 0.000312$  and  $\chi = 0.0177$ . Fig. 5(c) shows the simulation data via symbols and the corresponding RFOT theory plot of Eq. (B1) by lines; the theory agrees remarkably well in this regime with the simulation data.

### Appendix C: Confluency modification of $D_r$

We stated in the main text, Sec. III A, that the confluency modifies the rotational diffusivity of self-propulsion and leads to  $D_r^{\text{eff}}$  [Eq. (5)].  $D_r^{\text{eff}}$  enters the RFOT theory, and we have shown the comparison with simulation data in Figs. 3 and 4 in the main text. We show in Fig. 6 that this modification is crucial for agreement with the

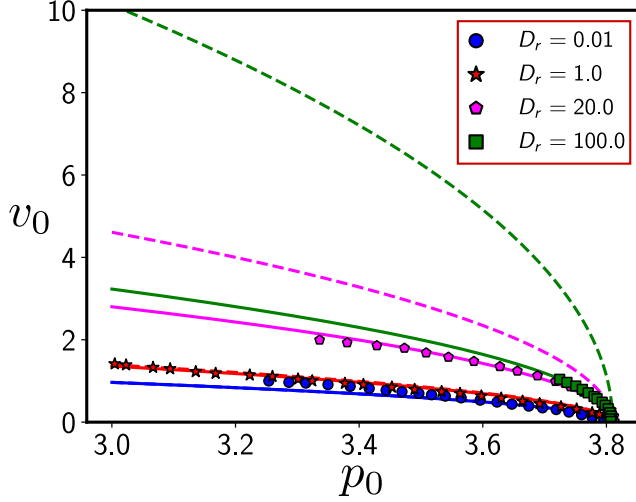


FIG. 6. We show the phase diagram in the  $v_0 - p_0$  plane for various  $D_r$  with (solid lines) and without (dashed lines) the confluency modification due to  $D_r$  [Eq. (5)]. The solid and dashed lines overlap for smaller values of  $D_r$ , but they deviate significantly from each other for higher values. The symbols represent the simulation data from Ref. [61] for the corresponding values of  $D_r$ .

simulation data. We present the  $v_0 - p_0$  phase diagrams at various  $D_r$  with this modification and without it (that is,  $\kappa_l = 0$  in Eq. (5)), by solid and dashed lines, respectively. Since  $D_r^{\text{eff}}$  is very close to  $D_r$ , they nearly agree with each other for  $D_r = 0.01$  and  $1.0$ . However, they deviate strongly for the higher values of  $D_r$ .

#### Appendix D: An alternative argument for the RFOT theory of confluent systems

We have argued, via existing and new simulation results, that the dynamics in confluent systems is sub-Arrhenius at larger values of  $p_0$ , and it becomes super-Arrhenius as  $p_0$  decreases. Furthermore, the application of the RFOT theory to the sub-Arrhenius regime leads to a negative effective Kauzmann temperature,  $T_K^{\text{eff}}$ . However,  $T_K^{\text{eff}}$  is positive in the super-Arrhenius regime, and the usual arguments of RFOT theory applies [72]. Based on this observation, we can develop a RFOT argument to extend the theory for such systems to understand the effect of  $p_0$ . Since this argument is specific to the confluent systems, for simplicity, we present it for equilibrium systems alone. The self-propulsion can be included in a similar way as discussed in the main text.

Within RFOT theory, the mosaic length is determined by the competition of an energy cost at the surface and gain in the bulk. The latter is governed by the configurational entropy,  $s_c$ , which determines the critical behavior. For the confluent systems,  $s_c \equiv s_c[\Phi(p_0)]$ . We

assume that for  $p_0 < p^*$ ,

$$s_c[\Phi(p_0)] = \begin{cases} c(p_0)[T - T_K(p_0)], & \text{when } T > T_K(p_0) \\ = 0, & \text{when } T < T_K(p_0) \end{cases} \quad (\text{D1})$$

where  $c(p_0)$  is a  $p_0$ -dependent constant.  $T_K(p_0)$  here also depends on  $p_0$  and we will obtain this dependence below.  $p^*$  gives the regime below which the theory is applicable. The simulation results show that  $p^*$  should be taken as  $p_0^{\text{ref}}$ , where the dynamics is Arrhenius-like. Thus, the theory should be applicable for values of  $p_0$  below  $p_0^{\text{ref}}$ . We assume that  $T_K(p_0)$  is a smooth function of  $p_0$  when  $p_0$  is close to  $p_0^{\text{ref}}$ , therefore, we can write

$$T_K(p_0) = -r(p_0 - p_0^{\text{ref}}), \quad (\text{D2})$$

where  $r$  is a positive constant. Thus, we have

$$s_c[\Phi(p_0)] = \begin{cases} c(p_0)[T + r(p_0 - p_0^{\text{ref}})], & \text{when } T > T_K(p_0) \\ = 0, & \text{when } T < T_K(p_0) \end{cases}.$$

Using this expression for  $s_c$  along with the arguments presented in Sec. III B, we obtain the RFOT theory for the confluent system in the absence of self-propulsion as

$$\ln\left(\frac{\tau}{\tau_0}\right) = \frac{E[1 - F(p_0 - p_0^{\text{ref}})]}{T + r(p_0 - p_0^{\text{ref}})}. \quad (\text{D3})$$

Note that this result is valid for  $T > T_K(p_0)$ . The system will have dynamics in this regime, and the dynamics freezes in the other regime.

#### Appendix E: Simulation details for the Vertex model

Here we provide additional details for the self-propelled Vertex Model (VM). To include self-propulsion, we associate each cell with a self-propulsion force  $\mathbf{f}_a$  of magnitude  $f_0$  (or velocity  $v_0$  considering  $\mu = 1$ ).  $\mathbf{f}_a$  acts along a polarity vector,  $\hat{\mathbf{n}}_i = (\cos \theta_i, \sin \theta_i)$ , where  $\theta_i$  is an angle measured from the  $x$ -axis. The total self-propulsion force on each vertex ( $k$ ),  $\mathbf{f}_a^k$ , is the mean self-propulsion forces of the 3 cells that share vertex  $k$ . We assume overdamped dynamics and write the equation of motion of vertex  $k$  as

$$\frac{d\mathbf{r}_k}{dt} = \mu^{-1}(\mathbf{F}_k + \mathbf{f}_a^k + \mathbf{F}_k^{\mathbf{R}}), \quad (\text{E1})$$

where  $\mathbf{F}_k = -\nabla_k \mathcal{H}$  is the force arising from the mechanical energy, Eq. (2), of the tissue.  $\mathbf{F}_k^{\mathbf{R}}$  is the random thermal noise with mean zero and standard deviation,  $\langle \mathbf{F}_i^{\mathbf{R}}(t) \mathbf{F}_j^{\mathbf{R}}(t') \rangle = 2k_B T \delta(t - t') \delta_{ij} \mathbf{I}$ , with  $\mathbf{I}$  being the unit tensor; we have set  $k_B$  to unity.  $\mathbf{f}_a^k$  is the active force acting on vertex  $k$ :  $\mathbf{f}_a^k = \frac{v_0}{3} \sum_{i \in \mathcal{N}(k)} \hat{\mathbf{n}}_i$ , where  $\mathcal{N}$  is the list of neighboring cells sharing vertex  $k$ .  $\theta_i(t)$  performs a rotational Brownian motion [Eq. (3)]. We have used the Euler-Murayama integration scheme to update

the discretized version of the equations (for each vertex).

To highlight the effects of activity, we have used  $T = 0$  in our simulations. Other parameters are as follows;  $\lambda_A = 1.0$ ,  $\lambda_P = 1.0$ ,  $A_{0\alpha} = 1.2$ ,  $A_{0\beta} = 0.8$ ,  $l_{T1} = 0.04$ ,  $\lambda_{T1} = 2.0$ ,  $\delta t = 0.01$ ,  $t_{T1} = 5\delta t$ . Our unit of length is  $\sqrt{\langle A_0 \rangle}$  and unit of time is  $\frac{1}{\mu\lambda_A\langle A_0 \rangle}$ . Unless otherwise specified, we have equilibrated the system for  $3 \times 10^5$  times before collecting the data, performed  $100t_0$  averaging and 32 ensemble averaging, and simulated 256 cells.

*Self-overlap function,  $Q(t)$* : In our simulations, we compute the center of mass,  $\mathbf{r}_i$ , for the cells from the positions of their vertices. We then define the self-overlap function,  $Q(t)$ , as

$$Q(t) = \left\langle \frac{1}{N} \sum_{i=1}^N W(a - |\mathbf{r}_i(t) - \mathbf{r}_i(0)|) \right\rangle, \quad (\text{E2})$$

where  $W(x)$  is the Heaviside step function:

$$W(x) = \begin{cases} 1 & \text{if } x > 0, \\ 0 & \text{otherwise.} \end{cases} \quad (\text{E3})$$

The parameter  $a$  is set to a constant value of 0.346 throughout the simulation. This value of  $a$  corresponds to the caging length scale of vibrational motions revealed via the MSD [inset of Fig. 3(b)]. The angular brackets denote initial time and ensemble averages. We define the structural relaxation time  $\tau$  as  $Q(t = \tau) = 0.3$ .

*Mean-square displacement,  $\Delta r^2(t)$* : We define  $\Delta r^2(t)$  as

$$\Delta r^2(t) = \left\langle \frac{1}{N} \sum_{i=1}^N (\mathbf{r}_i(t) - \mathbf{r}_i(0))^2 \right\rangle. \quad (\text{E4})$$

- 
- [1] D. T. Tambe, C. C. Hardin, T. E. Angelini, K. Rajendran, C. Y. Park, X. Serra-Picamal, E. H. Zhou, M. H. Zaman, J. P. Butler, D. A. Weitz, J. J. Fredberg, and X. Trepap, *Nat. Mater.* **10**, 469 (2011).
- [2] P. Friedl and D. Gilmour, *Nat. Rev. Mol. Cell Biol.* **10**, 445 (2009).
- [3] A. N. Malmi-Kakkada, X. Li, H. S. Samanta, S. Sinha, and D. Thirumalai, *Phys. Rev. X* **8**, 021025 (2018).
- [4] E.-M. Schötz, M. Lanio, J. A. Talbot, and M. L. Manning, *J. R. Soc. Interface* **10**, 20130726 (2013).
- [5] M. Poujade, E. Grasland-Mongrain, A. Hertzog, J. Jouanneau, P. Chavrier, B. Ladoux, A. Buguin, and P. Silberzan, *Proc. Natl. Acad. Sci. (USA)* **104**, 15988 (2007).
- [6] T. Das, K. Safferling, S. Rausch, N. Grabe, H. Boehm, and J. P. Spatz, *Nat. Cell Biol.* **17**, 276 (2015).
- [7] A. Brugués, E. Anon, V. Conte, J. H. Veldhuis, M. Gupta, J. Colombelli, J. J. Muñoz, G. W. Brodland, B. Ladoux, and X. Trepap, *Nat. Phys.* **10**, 683 (2014).
- [8] C. Malinverno, S. Corallino, F. Giavazzi, M. Bergert, Q. Li, M. Leoni, A. Disanza, E. Frittoli, A. Oldani, E. Martini, T. Lendenmann, G. Deflorian, G. V. Beznoussenko, D. Poulidakos, K. H. Ong, M. Uroz, X. Trepap, D. Parazzoli, P. Maiuri, W. Yu, A. Ferrari, R. Cerbino, and G. Scita, *Nat. Mater.* **16**, 587 (2017).
- [9] K.-J. Streitberger, L. Lilaj, F. Schrank, a. K.-T. H. Jürgen Braun, M. Reiss-Zimmermann, J. A. Käs, and I. Sack, *Proc. Natl. Acad. Sci. (USA)* **117**, 128 (2020).
- [10] P. Friedl and K. Wolf, *Nat. Rev. Cancer* **3**, 362 (2003).
- [11] L. Berthier and G. Biroli, *Rev. Mod. Phys.* **83**, 587 (2011).
- [12] P. Pareek, M. Adhikari, C. Dasgupta, and S. K. Nandi, *J. Chem. Phys.* **159**, 174503 (2023).
- [13] T. E. Angelini, E. Hannezo, X. Trepap, M. Marquez, J. J. Fredberg, and D. A. Weitz, *Proc. Natl. Acad. Sci. (USA)* **108**, 4717 (2011).
- [14] J.-A. Park, J. H. Kim, D. Bi, J. A. Mitchel, N. T. Qazvini, K. Tantisira, C. Y. Park, M. McGill, S.-H. Kim, B. Gweon, J. Notbohm, R. S. Jr, S. Burger, S. H. Randall, A. T. Kho, D. T. Tambe, C. Hardin, S. A. Shore, E. Israel, D. A. Weitz, D. J. Tschumperlin, E. P. Henske, S. T. Weiss, M. L. Manning, J. P. Butler, J. M. Drazen, and J. J. Fredberg, *Nat. Mater.* **14**, 1040 (2015).
- [15] K. D. Nnetu, M. Knorr, D. Strehle, M. Zink, and J. A. Käs, *Soft Matter* **8**, 6913 (2012).
- [16] B. Szabó, G. J. Szöllösi, B. Gönci, Z. Jurányi, D. Selmeczi, and T. Vicsek, *Phys. Rev. E* **74**, 061908 (2006).
- [17] X. Trepap, M. R. Wasserman, T. E. Angelini, E. Millet, D. A. Weitz, J. P. Butler, and J. J. Fredberg, *Nat. Phys.* **5**, 426 (2009).
- [18] F. Giavazzi, C. Malinverno, G. Scita, and R. Cerbino, *Front. Phys.* **6**, 120 (2018).
- [19] L. Atia, J. J. Fredberg, N. S. Gov, and A. F. Pegoraro, *Cells and Development* **168**, 203727 (2021).
- [20] K. Paul, S. K. Nandi, and S. Karmakar, *arXiv*, 2111.09829 (2021).
- [21] K. Paul, A. Mutneja, S. K. Nandi, and S. Karmakar, *Proc. Natl. Acad. Sci. (USA)* **120**, e2217073120 (2023).
- [22] J. Prost, F. Jülicher, and J. F. Joanny, *Nat. Phys.* **11**, 111 (2015).
- [23] J. Ranft, M. Basan, J. Elgeti, J.-F. Joanny, J. Prost, and F. Jülicher, *Proc. Natl. Acad. Sci. (USA)* **107**, 20863 (2010).
- [24] D. A. Matoz-Fernandez, K. Martens, R. Sknepnek, J. L. Barrat, and S. Henkes, *Soft Matter* **13**, 3205 (2017).
- [25] A. S. Alvarado and S. Yamanaka, *Cell* **157**, 110 (2014).
- [26] R. Farhadifar, J.-C. Röper, B. Aigouy, S. Eaton, and F. Jülicher, *Curr. Biol.* **17**, 2095 (2007).
- [27] S. Garcia, E. Hannezo, J. Elgeti, J. F. Joanny, P. Silberzan, and N. S. Gov, *Proc. Natl. Acad. Sci. (USA)* **112**, 15314 (2015).
- [28] S. Ramaswamy, *Annu. Rev. Condens. Matter Phys.* **1**, 323 (2010).
- [29] M. C. Marchetti, J. F. Joanny, S. Ramaswamy, T. B. Liverpool, J. Prost, M. Rao, and R. A. Simha, *Rev. Mod. Phys.* **85**, 1143 (2013).
- [30] L. M. C. Janssen, *J. Phys.: Condens. Matter* **31**, 503002 (2019).
- [31] L. Berthier, E. Flenner, and G. Szamel, *J. Chem. Phys.* **150**, 200901 (2019).
- [32] M. Paoluzzi, D. Levis, and I. Pagonabarraga, *Commun*

- Phys* **5**, 111 (2022).
- [33] J. Palacci, C. Cottin-Bizonne, C. Ybert, and L. Bocquet, *Phys. Rev. Lett.* **105**, 088304 (2010).
- [34] G. Szamel, *Phys. Rev. E* **90**, 012111 (2014).
- [35] M. Han, J. Yan, S. Granick, and E. Luijten, *Proc. Natl. Acad. Sci. (USA)* **114**, 7513 (2017).
- [36] E. Fodor, C. Nardini, M. E. Cates, J. Tailleur, P. Visco, and F. van Wijland, *Phys. Rev. Lett.* **117**, 038103 (2016).
- [37] G. Parisi, *Nature* **433**, 221 (2005).
- [38] L. Berthier, *Phys. Rev. Lett.* **112**, 220602 (2014).
- [39] R. Mandal, P. J. Bhuyan, M. Rao, and C. Dasgupta, *Soft Matter* **12**, 6268 (2016).
- [40] E. Flenner, G. Szamel, and L. Berthier, *Soft Matter* **12**, 7136 (2016).
- [41] R. Ni, M. A. C. Stuart, and M. Dijkstra, *Nat. Commun* **4**, 2704 (2013).
- [42] N. Klougnessa, F. Ginot, C. Ybert, C. Cottin-Bizonne, and M. Leocmach, *Phys. Rev. Lett.* **123**, 248004 (2019).
- [43] N. Klougnessa, F. Ginot, C. Ybert, C. Cottin-Bizonne, and M. Leocmach, *Phys. Rev. E* **100**, 062603 (2019).
- [44] P. Arora, A. K. Sood, and R. Ganapathy, *Phys. Rev. Lett.* **128**, 178002 (2022).
- [45] L. Berthier and J. Kurchan, *Nat. Phys.* **9**, 310 (2013).
- [46] G. Szamel, *Phys. Rev. E* **93**, 012603 (2016).
- [47] A. Liluashvili, J. Ónody, and T. Voigtmann, *Phys. Rev. E* **96**, 062608 (2017).
- [48] M. Feng and Z. Hou, *Soft Matter* **13**, 4464 (2017).
- [49] S. K. Nandi and N. S. Gov, *Soft Matter* **13**, 7609 (2017).
- [50] S. K. Nandi, R. Mandal, P. J. Bhuyan, C. Dasgupta, M. Rao, and N. S. Gov, *Proc. Natl. Acad. Sci. (USA)* **115**, 7688 (2018).
- [51] R. Mandal, S. K. Nandi, C. Dasgupta, P. Sollich, and N. S. Gov, *J. phys. commun.* **6**, 115001 (2022).
- [52] F. Graner and J. A. Glazier, *Phys. Rev. Lett.* **69**, 2013 (1992).
- [53] J. A. Glazier and F. Graner, *Phys. Rev. E* **47**, 2128 (1993).
- [54] P. Hogeweg, *J. Theor. Biol.* **203**, 317 (2000).
- [55] T. Hirashima, E. G. Rens, and R. M. H. Merks, *Develop. Growth Differ.* **59**, 329 (2017).
- [56] M. Chiang and D. Marenduzzo, *EPL (Europhysics Letters)* **116**, 28009 (2016).
- [57] S. Sadhukhan and S. K. Nandi, *Phys. Rev. E* **103**, 062403 (2021).
- [58] H. Honda and G. Eguchi, *J. Theor. Biol.* **84**, 575 (1980).
- [59] M. Marder, *Phys. Rev. A* **36**, 438(R) (1987).
- [60] A. G. Fletcher, M. Osterfield, R. E. Baker, and S. Y. Shvartsman, *Biophys. J.* **106**, 2291 (2014).
- [61] D. Bi, X. Yang, M. C. Marchetti, and M. L. Manning, *Phys. Rev. X* **6**, 021011 (2016).
- [62] Y.-W. Li, L. L. Y. Wei, M. Paoluzzi, and M. P. Ciamarra, *Phys. Rev. E* **103**, 022607 (2021).
- [63] M. Czajkowski, D. M. Sussman, M. C. Marchetti, and M. L. Manning, *Soft Matter* **15**, 9133 (2019).
- [64] M. Nonomura, *PLoS ONE* **7**, e33501 (2012).
- [65] B. Palmieri, Y. Bresler, D. Wirtz, and M. Grant, *Sci. Rep.* **5**, 11745 (2015).
- [66] B. Loewe, M. Chiang, D. Marenduzzo, and M. C. Marchetti, *Phys. Rev. Lett.* **125**, 038003 (2020).
- [67] D. Bi, J. H. Lopez, J. M. Schwarz, and M. L. Manning, *Soft Matter* **10**, 1885 (2014).
- [68] D. M. Sussman, M. Paoluzzi, M. C. Marchetti, and M. L. Manning, *Europhys. Lett.* **121**, 36001 (2018).
- [69] S. Sadhukhan and S. K. Nandi, *eLife* **11**, e76406 (2022).
- [70] V. Lubchenko and P. G. Wolynes, *Annu. Rev. Phys. Chem.* **58**, 235 (2007).
- [71] T. R. Kirkpatrick and D. Thirumalai, *Rev. Mod. Phys.* **87**, 183 (2015).
- [72] G. Biroli and J. P. Bouchaud, in *Structural Glasses and Supercooled Liquids: Theory, Experiment, and Applications*, edited by P. G. Wolynes and V. Lubchenko (2012).
- [73] D. Weaire and S. Hutzler, *The physics of foams* (Oxford University Press, 2001).
- [74] P. J. Albert and U. S. Schwarz, *Cell Adhesion & Migration* **10**, 516 (2016), pMID: 26838278.
- [75] D. L. Barton, S. Henkes, C. J. Weijer, and R. Sknepnek, *Plos Comput. Biol.* **13**, e1005569 (2017).
- [76] X. Yang, D. Bi, M. Czajkowski, M. Merkel, M. L. Manning, and M. C. Marchetti, *Proc. Natl. Acad. Sci. (USA)* **114**, 12663 (2017).
- [77] H. B. Wolff, L. A. Davidson, and R. M. H. Merks, *Bul. Math. Biol.* **81**, 3322 (2019).
- [78] M. Paoluzzi, L. Angelani, G. Gosti, M. C. Marchetti, I. Pagonabarraga, and G. Ruocco, *Phys. Rev. E* **104**, 044606 (2021).
- [79] D. P. Rivas, T. N. Shendruk, R. R. Henry, D. H. Reich, and R. L. Leheny, *Soft Matter* **16**, 9331 (2020).
- [80] L. Atia, D. Bi, Y. Sharma, J. A. Mitchel, B. Gweon, S. A. Koehler, S. J. DeCamp, B. Lan, J. H. Kim, R. Hirsch, A. F. Pegoraro, K. H. Lee, J. R. Starr, D. A. Weitz, A. C. Martin, J.-A. Park, J. P. Butler, and J. J. Fredberg, *Nat. Phys.* **14**, 613 (2018).
- [81] T. R. Kirkpatrick and P. G. Wolynes, *Phys. Rev. A* **35**, 3072 (1987).
- [82] T. R. Kirkpatrick, D. Thirumalai, and P. G. Wolynes, *Phys. Rev. A* **40**, 1045 (1989).
- [83] P. G. Wolynes and V. Lubchenko, *Structural Glasses and Supercooled Liquids* (John Wiley and Sons, Inc., Hoboken, New Jersey, 2012).
- [84] G. Parisi and F. Zamponi, *Rev. Mod. Phys.* **82**, 789 (2010).
- [85] W. Kauzmann, *Chemical Reviews* **43**, 219 (1948).
- [86] C. A. Angell, *J. Non-Cryst. Solids* **131-133**, 13 (1991).
- [87] C. A. Angell, *Science* **267**, 1924 (1995).
- [88] S. Gysin, M. Salt, A. Young, and F. McCormick, *Genes and Cancer* **2**, 359 (2011).
- [89] M. Rodrigues, N. Kosaric, C. A. Bonham, and G. C. Gurtner, *Physiol. Rev.* **99**, 665 (2019).
- [90] E. Bazellieres, V. Conte, A. Elosegui-Artola, X. Serra-Picamal, M. Bintanel-Morcillo, P. Roca-Cusachs, J. J. Muñoz, M. Sales-Pardo, R. Guimerà, and X. Trepat, *Nat. Cell Biol.* **17**, 409 (2015).
- [91] N. Gnan and E. Zaccarelli, *Nat. Phys.* **15**, 683 (2019).
- [92] L. Berthier and T. A. Witten, *Phys. Rev. E* **80**, 021502 (2009).
- [93] L. Berthier and T. A. Witten, *Europhys. Lett.* **86**, 10001 (2009).
- [94] M. Adhikari, S. Karmakar, and S. Sastry, *arXiv* , 2204.02936 (2022).
- [95] S. Pandey, S. Kolya, S. Sadhukhan, and S. K. Nandi, *arXiv* **v1**, 2306.07250 (2023).
- [96] P. Arora, S. Sadhukhan, S. K. Nandi, D. Bi, A. K. Sood, and R. Ganapathy, *arXiv* , 2401.13437 (2024).
- [97] V. Tarle, A. Ravasio, V. Hakim, and N. S. Gov, *Int. Biol.* **7**, 1218 (2015).
- [98] D. Sarkar, G. Gompper, and J. Elgeti, *Comm. Phys.* **4**, 36 (2021).

- [99] S. Tong, N. K. Singh, R. Sknepnek, and A. Košmrlj, *PLOS Comput. Biol.* **18**, 1 (2022).